Applied Catalysis A: General 388 (2010) 57–67

Contents lists available at ScienceDirect

Applied Catalysis A: General

journal homepage: www.elsevier.com/locate/apcata

Effects of pore diameter on particle size, phase, and turnover frequency in mesoporous silica supported cobalt Fischer–Tropsch catalysts

I.T. Ghampson[a,b,e], C. Newman[d,e], L. Kong[d,e], E. Pier[d,e], K.D. Hurley[a,e], R.A. Pollock[b,e,f], B.R. Walsh[b,c,e], B. Goundie[b,e,f], J. Wright[b,e,f], M.C. Wheeler[a,e], R.W. Meulenberg[b,e,f], W.J. DeSisto[a,b,e,f], B.G. Frederick[b,c,e,*], R.N. Austin[d,e,*]

[a] Department of Chemical and Biological Engineering, University of Maine, Jenness Hall, Orono, ME 04469, United States
[b] Laboratory for Surface Science and Technology, University of Maine, Orono, ME 04469, United States
[c] Department of Chemistry, University of Maine, Aubert Hall, Orono, ME 04469, United States
[d] Department of Chemistry, Bates College, Dana Chemistry Hall, Lewiston, ME 04240, United States
[e] Forest Bioproducts Research Institute, University of Maine, Orono, ME 04469, United States
[f] Department of Physics and Astronomy, University of Maine, Jenness Hall, Orono, ME 04469, United States

ARTICLE INFO

Article history:
Received 11 March 2010
Received in revised form 4 August 2010
Accepted 17 August 2010
Available online 24 August 2010

Keywords:
Fischer–Tropsch synthesis
Co heterogeneous catalyst
MCM-41
MCM-48
HMS
SBA15
X-ray diffraction
Turnover frequency
Pore size

ABSTRACT

A series of mesoporous silica supported cobalt catalysts for the Fischer–Tropsch reaction with pore diameters from 3 to 22 nm was synthesized and characterized. Detailed X-ray diffraction measurements were used to determine the composition and particle diameters of the metal fraction, analyzed as a three-phase system containing Co_{fcc}, Co_{hcp} and CoO. Catalyst properties were determined at three stages of catalyst history: (1) after the initial calcination step to thermally decompose the catalyst precursor into Co_3O_4, (2) after the hydrogen reduction step to activate the catalyst to Co and (3) after the FT reaction. Small Co_{hcp} particles were detected in all reduced catalysts contributing significantly to the Co surface area. The reaction rate increased with the pore diameter of the silica support. The results indicate the importance of careful catalyst characterization in determining the factors that contribute to reactivity. In addition, the identification of significant quantities of two cobalt metal phases suggests that further study of the intrinsic activity of each phase, as well as the structural features of the supports that determine the distribution of cobalt phases and particle sizes is warranted.

1. Introduction

Fischer–Tropsch synthesis (FTS) is receiving renewed attention, driven by the global need to convert non-petroleum based energy resources into fuels and chemicals. Cobalt catalysts are known to favor the production of higher molecular weight hydrocarbons in FTS and hence the characterization of cobalt-based catalysts supported on relatively high surface area materials has recently been the focus of intense research [1–7]. These materials have several key parameters that can be varied. Determining the influence of any one parameter on the overall reactivity of the catalysts has been challenging. The two factors that have received the most attention are the influence of metal particle size [1,5,8–11] and pore diameter [6,7,9,12–19]. Less attention has been focused on the influence of multiple Co phases [20–22]. In this paper we characterize a series of Co catalysts on porous silicas and demonstrate the presence of a substantial number of small Co_{hcp} particles. We suggest that a failure to account for cobalt in small particles can lead to an overestimation of the effectiveness of a catalyst and conclude that by accounting for both Co_{hcp} and Co_{fcc} surface areas, there is a clear correlation between turnover frequency (TOF) and pore diameter for support with 2–13 nm.

Turnover frequencies (moles of product produced – or substrate consumed – per surface metal per unit time) provide insight into which fundamental factors affect catalytic activity and can facilitate rational catalyst design. TOFs depend on estimates of surficial metal area, which are calculated using experimentally-measured average particle size [1,8,9,11,20,21,23]. Many authors calculate the surface area of Co FT catalysts based on the size of the Co_3O_4 particles (determined by XRD [1,9]) on as-prepared catalysts. However there is evidence that particle size and hence surface area may change during pretreatment. Prieto et al. found larger particles (18–71% larger) when looking at reduced catalysts (using chemisorption)

* Corresponding authors at: Department of Chemistry, Bates College, Dana Chemistry Hall, 5 Andrews Rd., Lewiston, ME 04240, United States. Tel.: +1 207 786 6295.
E-mail address: raustin@bates.edu (R.N. Austin).

0926-860X/$ – see front matter © 2010 Elsevier B.V. All rights reserved.
doi:10.1016/j.apcata.2010.08.028

relative to oxidized material (by XRD) which they attribute to sintering of particles during reduction [24]. Song and Li showed that estimates of particle diameters vary dramatically when incomplete reduction of Co_3O_4 particles is taken into account [19].

In general, FTS has been thought to be insensitive to structure [7] but there are some data that suggest that very small metal particles (below a critical threshold of approximately 7–10 nm) lead to less effective catalysts [7,10,11,25]. Small particles might be less active because they contain fewer edge defects where catalysis can more easily occur [10], because they contain more low coordinate Co that might bind reactants more tightly and slow reaction rates [25], or because the high surface area could destabilize the particles and prevent reduction [3,9,14] or promote reoxidation [1]. Some experiments suggest a particle size threshold (approximately 10 nm) above which TOF are unchanged [2].

Furthermore, several researchers have noted that after reduction multiple metal phases can exist, which could affect reactivity [10]. Srinivasan et al. [22] and Enache et al. [21] found both fcc and hcp phases after reduction. Enache et al. noted higher TOF with materials that contained more Co_{hcp} than materials with more Co_{fcp} [21], but thought that this might be due to defects and disorder [21]. Ducreux et al. were able to preferentially prepare the hcp phase by reducing Co_2C precursors and found that predominantly hcp material converted almost two times as much CO as the predominantly fcp material [20].

In this paper, we describe the characterization of cobalt metal catalysts analyzed with XRD as CoO and two metal phases: Co_{fcc} and Co_{hcp} and report on the relationships between metal phases, particle diameters, support pore diameters and turnover frequencies for nine different catalysts. Additional characterization with nitrogen porosimetry, X-ray absorption near edge structure (XANES), and transmission electron microscopy/selected area diffraction (TEM/SAD) supports our materials analysis. Cobalt catalysts were impregnated onto silica supports with different pore diameters and calcined to yield Co_3O_4 particles, reduced with hydrogen to produce CoO and Co metal, and then exposed to FTS conditions for 10 h. We characterized the catalyst properties at three different stages in catalyst history: (1) after calcination, (2) after H_2 reduction and (3) after FT reaction. X-ray diffraction data was used to determine the particle diameters of Co_3O_4 (Stage 1) and Co_{hcp}, Co_{fcc} and CoO (Stages 2 and 3) as well as the relative amounts of Co_{hcp}, Co_{fcc} and CoO at Stages 2 and 3.

The most notable relationship we find is that turnover frequencies, based upon total metal surface areas determined after FTS, are very well correlated with pore diameter. We also note that significant changes in dispersion occurred during the 10 h time under reaction conditions. Hence a failure to account for cobalt in small particles can lead to an overestimation of the effectiveness of a catalyst. We also find evidence that solid supports with extensive networks of small micropores may decrease the overall efficiency of FT catalysts.

2. Experimental

2.1. Materials and methods

Ammonium hydroxide (NH_4OH, 28%) and hydrochloric acid (HCl, 37%) were obtained from Fischer Scientific. Cetyltrimethylammonium chloride (CTMACl, 25%), cetyltrimethylammonium bromide (CTMABr), hexadecylamine (HDA) and tetraethylorthosilicate (TEOS, 99%) were obtained from Aldrich. Tetramethylammonium hydroxide pentahydrate (97%), cobalt(II)nitrate hexahydrate and ethanol (EtOH, 99.5%) were obtained from Acros Organics. Cabo-sil M5 fumed silica (200 m^2/g (BET) 0.2–0.3 μm particle size, >99.8% SiO_2) was obtained from Cabot, poly(ethylene oxide)–poly(propylene oxide)–poly(ethylene oxide) (M_r = 5750, $EO_{20}PO_{70}EO_{20}$, Pluronic P123) was obtained from BASF. All materials in this work were used without further purification.

2.2. Catalyst synthesis

2.2.1. Synthesis of silica supports

MCM-41 was synthesized following a literature procedure [26], in which 28% NH_4OH (1 g, 28.53 mmol) was mixed with the surfactant, a 25% solution of CTMACl (21 g, 65.63 mmol). The solution was then added to tetramethylammonium hydroxide pentahydrate (5.3 g, 29.24 mmol). Cabo-sil M-5 fumed silica (5.6 g, 27.6 mmol) and deionized water (11.4 g, 633.33 mmol) were subsequently added to the mixture, and the solution was stirred at room temperature for 30 min. The mixture was then transferred to a polymer flask, sealed and heated at 373 K for 24 h in an oven. After filtration and washing with deionized water, the solid product recovered was air-dried at room temperature for 24 h. The sample was then calcined in air by a ramp of 1 K/min to 773 K and held at 773 K for 6 h.

MCM-48 was synthesized by a conventional hydrothermal pathway [27]. CTMABr (2.4 g, 6.6 mmol) was dissolved in 50 mL Milli-Q water. Ethanol (50 mL) and NH_4OH (5N solution, 12 mL) were then added, and the solution stirred for 10 min. TEOS (3.64 mL, 16.3 mmol) was added and the reaction stirred for 2 h. The solid product was recovered by filtration, rinsed with Milli-Q water and then calcined for 6 h at 823 K.

For the preparation of HMS [28], hexadecylamine (0.80 g, 3.33 mmol) was added, at room temperature, to a solution of Milli-Q water (6.3 mL) and ethanol (99.5%, 4.1 mL) and stirred until a homogenous mixture was obtained. TEOS (2.23 mL) was then added under vigorous stirring. The reaction was stirred overnight and the solid was recovered by centrifugation. The solid product was washed with Milli-Q water during vacuum filtration, air-dried at room temperature and calcined at 823 K for 10 h.

SBA-15 was synthesized using a non-ionic surfactant as the structure-directing agent according to reported procedure [29,30] as follows: amphiphilic difunctional block copolymer, pluronic P123 (6 g, 1.04 mmol) was dissolved in deionized water (45 g, 2500 mmol) and 2 M HCl solution (180 g, 4931.5 mmol) with stirring. Then, TEOS (12.75 g, 61.20 mmol) was added to the solution with stirring at 313 K for 24 h. The homogeneous gel mixture was then transferred into a polymer flask, sealed and heated at 373 K for 48 h. After filtration and washing with water, the white solid product recovered was air-dried at room temperature for 24 h. The sample was then calcined in air by a ramp of 1 K/min to 773 K and held for 10 h.

The synthesis of cobalt incorporated MCM-48 (Co-MCM-48) used the same procedure as that used to prepare MCM-48 except $Co(NO_3)_2{\cdot}6H_2O$ (0.47 g, 1.33 mmol) was added before the addition of ethanol and NH_4OH.

Cobalt modified HMS (Co-HMS) was prepared by following the same procedure used to prepare HMS except $Co(NO_3)_2{\cdot}6H_2O$ (0.291 g, 1.00 mmol) was added before the addition of TEOS.

Cobalt modified SBA-15 (Co-SBA-15) was prepared using the same procedure used to prepare SBA-15 except that $Co(NO_3)_2{\cdot}6H_2O$ (1.886 g, 6.48 mmol) as added with TEOS.

Two sources of commercial silica gel were also used as supports: silica gels from Qingdao Haiyang Chemical Ltd. (silica gel no. 775, 30–50 mesh, 300–700 μm particle size) and silica gel granules from Grace Davison (silica gel no. 646, 35–60 mesh).

2.2.2. Synthesis and metal determination of catalysts

All of the supports were impregnated using a one-step wetness impregnation method where an appropriate amount of cobalt nitrate, corresponding to a nominal 9.1 wt.% Co metal content in

the final catalysts, was dissolved in excess water and added to the support. The mixture was then left overnight at ambient temperature. After impregnation, the samples were dried at 373 K for 12 h, and subsequently calcined in a flow of dry air by a ramp of 1 K/min to 773 K and held for 5 h (Stage 1 in catalyst history). They were then pressed and sieved to obtain 180–450 μm particle size. Cobalt metal loading was determined by ICP-OES (using a Perkin Elmer Optima 3000 XL) or by Galbraith Laboratories using ICP-MS. Samples analyzed in-house were digested in a microwave digester using concentrated nitric acid and hydrochloric acid. In-house results gave good agreement with those from Galbraith.

Overall, the supports have very similar chemical properties. Silica MCM-41 [31–33], MCM-48 [34], SBA-15 [35], and HMS [36] are minimally acidic, especially in comparison to alumina or alumina-doped supports. Silica gel has also been shown to be less acidic than HZSM-5 and tungsten-doped silica gels [37]. Incorporation of heteroatoms into a silica framework has been reported to increase thermal stability [38–41] and may also increase the acidity of the supports [4,28]. Experiments to test these hypothesis are underway.

Data for the following catalysts are reported in this paper: Co/MCM-41, Co/MCM-48, Co/Co-MCM-48, Co/HMS, Co/Co-HMS, Co/SBA-15 Co/Co-SBA-15 Co/silica gel no. 775, Co/silica gel no. 646, where the "/Co-X" indicates cobalt incorporation into the framework.

2.3. Nitrogen porosimetry

Nitrogen sorption isotherms were measured at 77 K using a Micromeritics ASAP-2020; surface area, pore size and pore volume analyses were done using the Micromeritics software. Prior to analysis the samples were outgassed under vacuum. MCM-41 was outgassed at 623 K for 10 h while all other mesoporous silica supports and Co impregnated supports were outgassed at 523 K for 8 h.

The specific surface area, pore volume and average pore diameter were calculated using standard approaches. The BET specific surface area [42] was calculated using the adsorption branch of the nitrogen sorption isotherm in the relative pressure range of 0.05–0.25 (P/P_0) and the total pore volume was recorded at $P/P_0 = 0.995$. Pore size distributions were calculated via the adsorption branch of the nitrogen sorption isotherm using the BJH method [43], based on the Kelvin equation. However, the Kelvin equation and statistical film thickness curve used for analysis were modified to those reported by Kruk et al. [44] (Eqs. (1) and (2) respectively):

$$r\left(\frac{p}{p_0}\right) = \frac{2\gamma V_L}{RT\,\ln(p/p_0)} + t\left(\frac{p}{p_0}\right) + 0.3\,\text{nm} \quad (1)$$

$$t\left(\frac{p}{p_0}\right) = 0.1\left[\frac{60.65}{0.0307.01 - \log\ (p/p_0)}\right]^{0.3968} \quad (2)$$

2.4. Catalysts treatment

Catalyst material properties are reported in this paper in relation to three different stages in the catalyst history to develop a picture of how these materials change in the presence of high temperatures and hydrogen pressures and in the course of catalyzing FTS. Stage 1 is the as-prepared catalyst, after calcination. Stage 2 is after the catalysts were reduced, but prior to FT synthesis. Stage 3 is after Fischer–Tropsch synthesis. All treatments were carried out in an Altamira AMI-200 R-HP catalyst characterization instrument.

For Stage 1, 200 mg of each catalyst was calcined in air at 773 K for 5 h before characterization with XRD and BET. For Stage 2, 100 mg of catalyst was calcined in air at 773 K for 5 h, followed by reduction in 10% H_2/90% Ar at 773 K for 5 h. The sample was cooled down to ambient temperature in Ar and then characterized. For Stage 3, 100 mg of catalyst was calcined in air at 773 K for 5 h, followed by reduction in 10% H_2/90% Ar at 773 K for 5 h. The sample was cooled down to ambient temperature in Ar, followed by measurement of the activity in Fischer–Tropsch synthesis at 543 K and 10 bar for 10 h. The sample was cooled down to ambient temperature in the reactant gas mixtures (10% CO/He and 10% H_2/Ar) and then characterized immediately with XRD.

2.5. Fischer–Tropsch synthesis (FTS)

Fischer–Tropsch synthesis was performed at 543 K and 10 bar in an Altamira AMI-200 R-HP characterization instrument. During the FT synthesis two independently controlled gas mixtures, 10% CO in He and 10% H_2 in Ar (with a 1:2.1 mole ratio), were fed to the catalyst in an up-flow configuration. The reactor was pressurized and then heated at 10 K/min to 543 K where it was held for 10 h. The product stream was sampled through a 1 m long 50 μm ID capillary into a turbo-molecular pump station (AMATEK) and analyzed with an SRS RGA-300 Mass Spectrometer. Typically, 100 mg of catalyst was packed into a 1/4-inch glass-lined stainless steel reactor tube connected via Swagelock fittings. The thermocouple probe is in contact with the top of the catalyst bed to control the reactor temperature. The moles of reactants consumed were calculated from the change in CO/He and H_2/Ar ratios, using the inert gases as internal standards, and was less than 10%. The conversion of CO typically increased over a period of several hours; the steady state reaction rates reported correspond to activity after 10 h on-stream. After reaction, separate portions of the catalysts were taken immediately for X-ray diffraction measurement or stored in glass ampoules under vacuum for XANES measurements at the beamline.

2.6. XRD (phase identification and particle size)

Wide angle θ–2θ X-ray diffraction patterns for Co, CoO and Co_3O_4 phase identification and particle size determination were acquired at room temperature on a PANalytical X'PertPro X-ray diffractometer utilizing Cu K_α radiation. The incident beam was focused in line mode through a 0.145 mm Ni automatic attenuator, a 1/2° divergence slit, and a 15 mm beam mask following reflection off a parabolic W/Si mirror. To limit the Co fluorescence contribution to background, the diffracted beam was directed sequentially through a 0.27° parallel plate collimator, a 0.04 radian Söller slit assembly, and a (0 0 2) graphite monochromator before reaching the proportional detector. The standard scan parameters for Co_3O_4 (Stage 1) were to scan from 15 to 70° 2θ with a step size of 0.03° and a counting time of 1 s per step. For Co and CoO (determined at Stages 2 and 3, respectively) the samples were scanned from 30 to 160° 2θ, with a step size of 0.03° and a counting time of 7 s per step. The powder catalyst samples (100 mg) were cast onto zero background single crystal quartz plates cut 6° off (0 0 1) as slurries in 2-propanol and, to avoid air oxidation, measured immediately following reduction or exposure to Fischer–Tropsch conditions. There was no evidence of initial oxidation of the catalysts during XRD measurements. However, if the catalysts were exposed to air for several days, slow oxidation of the cobalt was visible by XRD. This observation is consistent with other studies in which a surface wax product layer is thought to build up after several hours of FTS, protecting the cobalt particles from oxidation [45–47].

The instrumental contribution to line broadening was accounted for by measuring a LaB_6 standard (NIST SRM 660) from 20 to 140° 2θ using an identical optical configuration to that used for data collection on the catalyst samples, followed by Rietveld refinement on the entire spectrum using EXPGUI graphical interface for General Structural Analysis System (GSAS) package [48,49]. In the GSAS program, the diffraction line positions and intensities are calculated directly from the unit cell and

Table 1
Phases analyzed at three stages of catalysts history and their structures and lattice parameters.

Phases/Stages	Space group	Lattice parameters (Å)		
		a	*b*	*c*
Co_3O_4/Stage 1	*Fd−3m*	8.084	8.084	8.084
Co_{fcc}/Stages 2 and 3	*Fm−3m*	3.545	3.545	3.545
Co_{hcp}/Stages 2 and 3	*P63/mmc*	2.503	2.503	4.060
CoO/Stages 2 and 3	*Fm−3m*	4.260	4.260	4.260

the lineshape accounts for particle size, strain, and preferential orientation effects. The contributions of the silica support to the diffraction pattern were accounted for by measuring wide angle XRD patterns of SBA-15, HMS and MCM-48 silica materials and using them as background by fitting the amorphous scattering with a non-linear function (a 12-term shifted Chebyschev polynomial). The symmetry and lattice parameters of the phases analyzed are shown in Table 1.

Quantification of the relative amount of each phase present in the catalyst samples at Stages 2 and 3 were determined from XRD data. The peak intensity of the kth line of phase α was calculated using $I_k = S_\alpha M_k L_k |F_k|^2$, where S_α is the scale factor for phase α, M_k is the multiplicity, L_k is the Lorentz Polarization Factor and F_k is the structure factor of the kth diffraction line. The weight fraction of phase α was calculated using $W_\alpha = (S_\alpha X_\alpha MW_\alpha V_\alpha)/\sum_i (S_i Z_i MW_i V_i)$ where Z is the number of formula units per unit cell, MW is the molecular weight and V is the unit cell volume. This method was validated by analyzing the ratio of Co_{hcp}/Co_{fcc} in a standard (Alfa-Aesar, 22 mesh, 99.9998%). Our results were in excellent agreement with the published ratio [50].

Quantitative XRD analysis allows us to determine both the particle size and relative amounts of each phase. It gives significantly different total surface areas from stage to stage in catalyst history; consequently, the calculated TOF varies significantly depending on the stage in catalyst history upon which the specific metal surface area is based.

2.7. Transmission electron microscopy (TEM) and selected area diffraction (SAD)

Freshly prepared catalysts were examined using TEM and selected area diffraction (SAD) with a Phillips CM 10 microscope at 100 keV. Samples were ground and electrostatically transferred onto carbon-coated grids. Images were recorded on Kodak 4489 electron image film.

2.8. X-ray absorption spectroscopy (XAS)

For the characterization of the local electronic structure of cobalt in the catalysts, synchrotron based X-ray absorption near edge spectroscopy (XANES) measurements were performed. The XANES spectra were acquired at the bend magnet beamline 8-2 at the Stanford Synchrotron Radiation Laboratory. The powder catalyst samples were deposited on carbon tape onto a stainless steel sample holder. A consistent powder thickness was maintained from sample to sample. For analysis of post-temperature programmed reduction (TPR) or post-FTS samples, the reacted materials were vacuum-sealed in an ampoule upon completion of the reaction. The vacuum-sealed samples were unpacked under ambient conditions at the synchrotron beamline, mounted onto carbon tape and immediately loaded into the UHV chamber. Total time of exposure to air was less than 1 min (less than the time exposed to air during the XRD experiments). Experimental measurements were taken at base pressures of less than 5×10^{-9} Torr. XAS experiments were conducted using the total electron yield (TEY) detection method where the total photocurrent is measured as the photon energy is scanned through the absorption edges. All spectra are normalized to the photocurrent from a gold grid. The experimental energy resolution is ~0.15 eV at the cobalt L_3-edge.

Table 3
Particle size of Co_3O_4 at Stage 1 and predicted metal size and dispersion of Co(0) after reduction.

Catalyst	Particle size (nm)		Percent reduction (%) in Stage 2	Expected dispersion (%)
	Co_3O_4	Co(0)		
Co/MCM-41	10.4	7.8	86.3	12.3
Co/MCM-48	4.8	3.6	28.4	26.6
Co/Co-MCM-48	30.9	23.2	53.9	4.1
Co/HMS	19.9	14.9	48.2	6.4
Co/Co-HMS	32.5	24.4	58.5	4.0
Co/SBA-15	10.0	7.5	83.4	12.9
Co/Co-SBA-15	14.9	11.1	78.5	8.6
Co/silica gel no. 775	12.4	9.3	96.4	10.4
Co/silica gel no. 646	17.9	13.5	94.7	7.1

3. Results

3.1. Materials characterization

Table 2 provides the characterization data of the silica supports used in this study. The surface areas of the supports ranged from 300 to 1400 $m^2\,g^{-1}$ and the total pore volumes (TPV) ranged from 0.67 to 1.2 $cm^3\,g^{-1}$. The primary pore diameters were estimated from the maximum in the BJH pore size distribution. For these supports the primary pore diameters varied from 3.2 to 2 nm. After impregnation and calcination, the surface areas decreased.

For particle size determination and phase identification, a detailed peak shape analysis of the XRD pattern was performed after all three stages of catalyst history. These were done by Rietveld refinements of the scale factor, background coefficients, unit cell lattice constants and profile-function coefficients in GSAS. Atomic coordinates within the cell, site fractions, and thermal motion

Table 2
Catalysts used in this study.

Silica support (without cobalt)				Silica supported cobalt catalysts		
Sample	S_{area} (m^2/g)	TPV (cm^3/g)	d_{pore} (nm)	S_{area} (m^2/g)	TPV (cm^3/g)	d_{pore} (nm)
Co/MCM-41	978	0.67	3.2	510	0.49	3.8
Co/MCM-48	1392	0.83	3.3	1152	0.62	3.1
Co/Co-MCM-48	941	0.71	3.5	495	0.49	2.9
Co/HMS	1001	1.31	4.6	783	0.88	4.3
Co/Co-HMS	515	0.63	3.8	431	0.62	3.7
Co/SBA-15	885	1.21	10.0	613	1.02	10.4
Co/Co-SBA-15	933	1.07	9.4	632	0.89	9.8
Co/silica gel no. 775	464	1.07	13.0	343	0.87	14.2
Co/silica gel no. 646	307	1.20	22.3	302	1.18	21.7

parameters were kept fixed during the refinement. Effects of preferred orientation and shape anisotropy were significant in the hcp phase. For comparison with previous studies [5,9,51,52], we measured the XRD after air-calcination to estimate Co_3O_4 particle size at Stage 1. Table 3 provides the particle size and dispersion of the cobalt metal, along with the percent reduction observed at Stage 2, to calculate specific surface areas that would be expected after reduction. The Co_3O_4 particle diameter was calculated from the GSAS fit to the XRD data.[1] The cobalt metal particle size expected after reduction was calculated by scaling the Co_3O_4 particle size by 0.75 [9]. The cobalt metal particle diameter (d) was used to calculate the dispersion using the relation $D = 96/d$ (nm) for spherical cobalt particles, assuming a site density of 14.6 atoms nm^{-2} [9]. The dispersion values calculated from Stage 1 data were fairly constant for all the catalysts used in our study.

Careful analysis of the XRD data after hydrogen reduction (pre-reaction Stage 2) and post-reaction (Stage 3) enabled us to detect the presence of two cobalt phases (fcc and hcp) as well as a CoO phase and to determine the particle size of all three particle types. Fig. 1A shows the entire XRD pattern after air-calcination of Co/Co-HMS from 30 to 160° 2θ along with the Reitveld refinement fit and residuals. Reitveld refinement for samples after H_2 reduction and FT catalytic testing was performed with all three phases over the entire range, which allowed particle sizes of each phase to be determined. For CoO and Co_{fcc}, there was no significant particle size anisotropy or preferential orientation. For Co_{hcp}, refinement of both particle size anisotropy and preferential orientation parameters significantly improved the fit.[2] For the Co_{hcp} particles, the dispersion was calculated from the components parallel $d_{||}$, and perpendicular $d_{\perp}$, to the c axis of a cylindrical particle using the relation:

$$D_{cyl} = \frac{0.321 d_{\perp}(\text{nm}) + 0.642 d_{||}(\text{nm})}{d_{\perp}(\text{nm}) d_{||}(\text{nm})}$$

Fig. 1B and C shows expanded regions of the XRD patterns of Co/silica gel no. 646 and Co/SBA-15 taken at Stage 3. The fitted profiles for each individual phase are shown along with the sum to fit the entire diffraction data. For Co/silica gel no. 646, the narrow peak at 44.3° corresponds to large fcc particles. The hcp peak at 47.0° and all related hcp lines are substantially broader, indicating much smaller particle sizes. By contrast, in the Co/SBA-15, the broad Co_{hcp} peak at 47° is not as apparent, because it is so broad and is masked by the tails of the adjacent CoO and Co_{fcc} peaks.

TEM measurements were made on the Co/silica gel no. 646 catalyst at Stage 2 and the data obtained from this technique supports the phases observed in the XRD data. Fig. 2 shows a TEM image revealing darker striations suggesting the presence of cobalt within the pore structure, although individual particles could not be resolved. Analysis of the corresponding selected area diffraction pattern gave all of the major lines in XRD for the hcp phase. The d-spacings correlated closely with those determined by XRD ($R^2 = 0.9992$). The diffraction patterns obtained were always identified as the hcp phase. We were not able to identify large metal particles or diffraction patterns associated with the fcc phase, but the relative number of fcc particles should be small compared to the number of hcp particles.

Table 4 shows the relative amounts of each phase in each supported catalyst at Stage 2 (also plotted in Fig. 3 against support

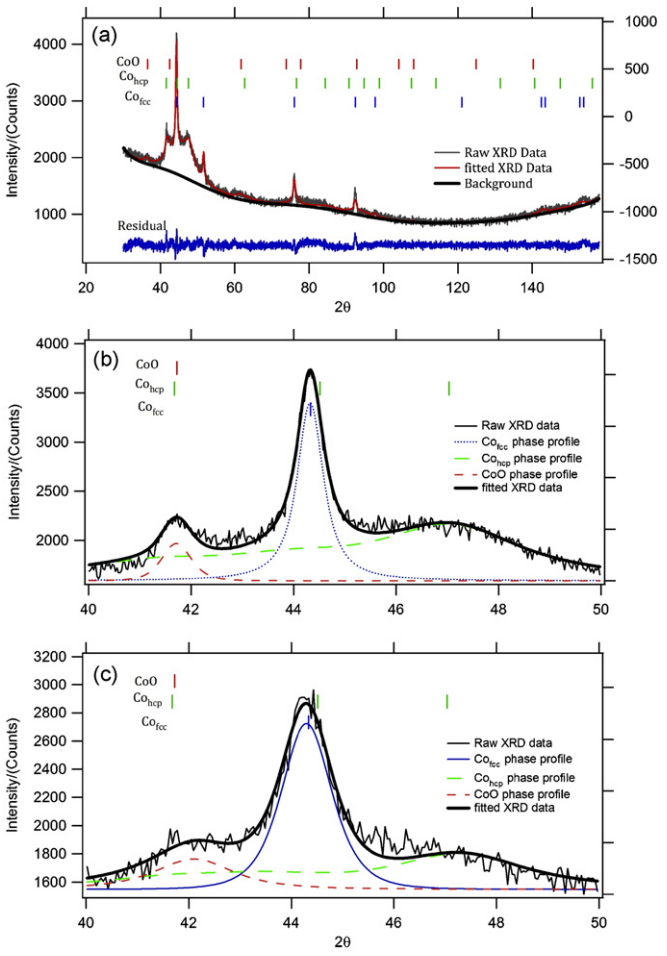

Fig. 1. (A) The full XRD pattern for Co/Co-HMS post-FT, fit using Reitveld refinement of the three phases CoO, Co_{hcp}, and Co_{fcc} and a Chebyschev background determined from the amorphous silica support, showing sharp Co_{fcc} lines and broad CoO and Co_{hcp} lines corresponding to smaller particles. Markers indicate the positions of lines unique to each phase. Expanded region showing the fcc, hcp and CoO lines for (B) Co/silica no. 646 and (C) Co/SBA-15.

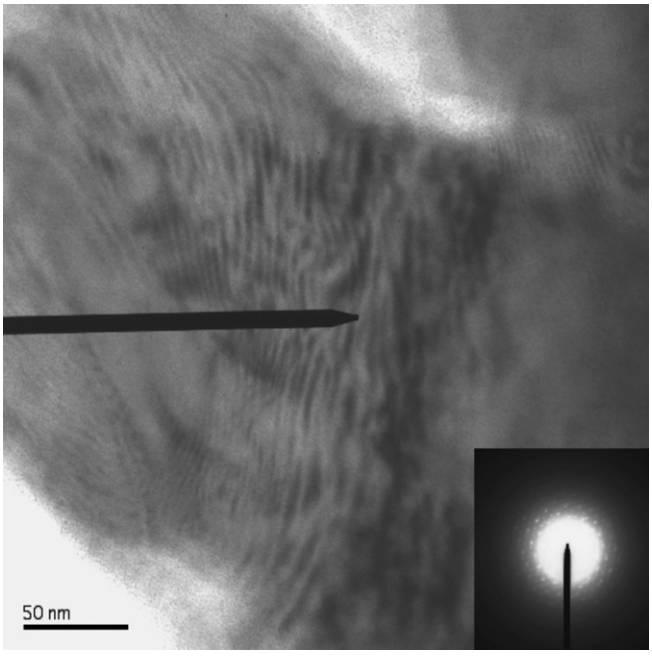

Fig. 2. TEM image of a region of catalyst Co/silica no. 775 with the corresponding Co_{hcp} diffraction pattern.

[1] The particle size broadening for CoO and Co(fcc) was estimated from the $1/\cos(\theta)$ dependent term of the Lorentzian broadening of the continuous wave (CW) peak profile function 2 in GSAS.

[2] The particle size parallel to the c axis was determined from the Lorentzian Scherrer term ($1/\cos(\theta)$), while the size perpendicular was calculated from the $\cos(\phi)/\cos(\theta)$ term. The isotropic Lorentzian strain broadening term ($\tan(\theta)$) was varied but the calculated strain was only a few percent.

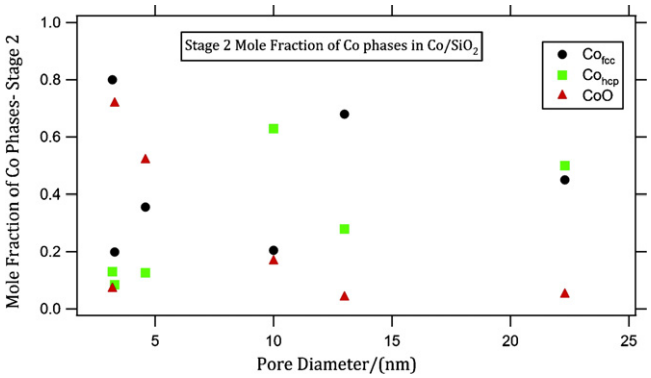

Fig. 3. Mole fraction of cobalt phases for catalysts after reduction in hydrogen (Stage 2) showing a systematic decrease in CoO with increasing pore diameter, but no clear dependence of the relative amounts of Co_{hcp} and Co_{fcc}.

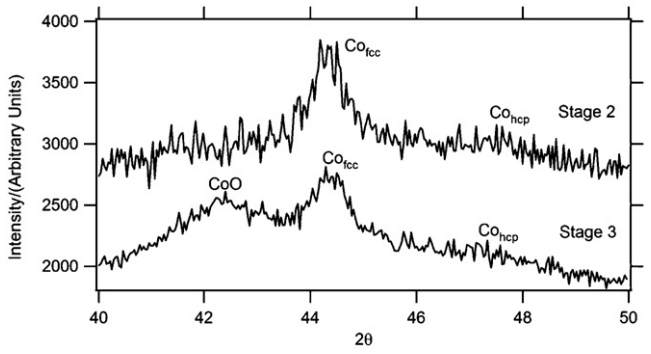

Fig. 4. XRD pattern illustrating the increase in the amount of CoO before (Stage 2) and after (Stage 3) reaction under FTS conditions for the small pore diameter catalyst Co/MCM-41.

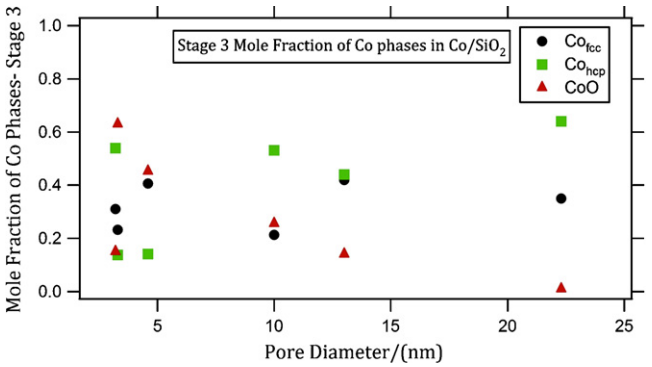

Fig. 5. Mole fraction of cobalt phases for catalysts after reaction for 10 h in FTS (Stage 3) showing a systematic decrease in CoO with increasing pore diameter, but no clear dependence of the relative amounts of hcp and fcc phases.

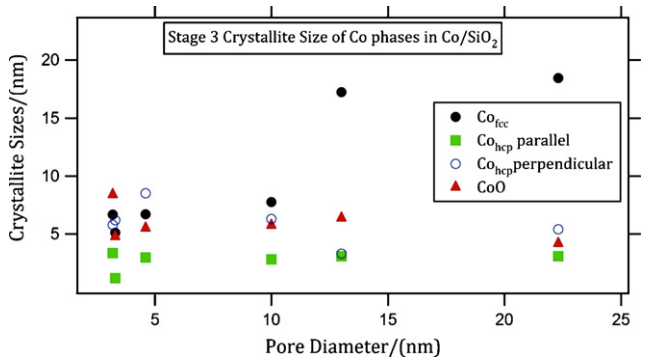

Fig. 6. Crystalite size for catalysts from XRD Reitveld refinement of the indicated phases showing the small and constant size of Co_{hcp} particles, while the size of Co_{fcc} particles increased with support pore diameter.

pore diameter). The relative amounts of Co_{hcp} and Co_{fcc} for the different supported catalysts at this stage show no relationship to pore diameter. Apart from the Co/MCM-41 catalyst, the CoO mole fraction decreases monotonically with pore diameter. Particle sizes and dispersion, calculated from the XRD data, are also given in Table 4. The Co_{hcp} particle size remains small and fairly constant while the Co_{fcc} particle size decreases with decreasing support pore diameter. The CoO particle size does not show a dependence on support pore diameter.

Table 5 shows the relative amounts of each phase in each supported catalyst at Stage 3. The relative amount of CoO present after 10 h under FTS conditions still generally decreases with increasing pore diameter. In the larger pore size catalysts, the relative amount of CoO decreases, while in the smaller pore diameter supports, it increases. Fig. 4 shows the expanded region of XRD spectra showing the evolution of CoO. In this case, the CoO peak at 42° grows while the Co_{fcc} peak at 44.3° diminishes. The Co_{hcp} peak at 47° remains fairly constant. Although the mole fraction of CoO varies with pore diameter, the relative amounts of Co_{fcc} and Co_{hcp} do not show any clear dependence on the support pore diameter, as shown in Fig. 5. XRD data used to calculate particle sizes and dispersion at Stage 3 are given in Table 5 and shown in Fig. 6. Similar to the Stage 2 data, the Co_{hcp} particle size remains small and fairly constant while the Co_{fcc} particle size decreases with decreasing support pore diameter. The CoO particle size is also relatively insensitive to pore diameter and generally smaller than the Co_{fcc} particles. The Co_{hcp} and Co_{fcc} dispersion values are calculated from the particle sizes and mole fraction determined from the XRD data.

Because our XRD analysis only quantified the material in ordered crystalline cobalt phases, XANES measurements were made to provide complementary information regarding the pres-

Table 4
Mole fractions (χ), particle sizes and dispersion of Co_{fcc} and Co_{hcp} for Stage 2.

Catalyst	Mole ratio			Particle size (nm)				Dispersion (%)		
	FCC Co^0	HCP Co^0	CoO	FCC Co^0	HCP Co^0		CoO	FCC Co^0	HCP Co^0	Weighted sum
					P_{II}	$P_{\perp}$				
Co/MCM-41	0.80	0.13	0.07	7.5	3.6	7.2	3.9	12.8	17.7	15.3
Co/MCM-48	0.20	0.08	0.72	4.7	1.2	4.4	6.6	20.4	41.7	26.8
Co/Co-MCM-48	0.24	0.30	0.46	29.8	1.2	4.2	5.2	3.2	42.2	24.8
Co/HMS	0.35	0.13	0.52	8.1	3.8	6.3	7.5	12.0	18.5	13.7
Co/Co-HMS	0.20	0.39	0.41	3.0	1.6	7.5	8.9	3.3	27.8	19.9
Co/SBA-15	0.21	0.63	0.17	8.2	4.0	8.3	8.9	11.7	15.8	14.8
Co/Co-SBA-15	0.07	0.72	0.21	9.4	1.4	4.1	8.1	10.2	39.4	37.7
Co/silica gel no. 775	0.68	0.28	0.04	9.5	3.8	6.6	9.5	10.1	18.1	12.4
Co/silica gel no. 646	0.45	0.50	0.05	22.0	3.7	6.2	7.8	4.3	19.0	12.0

Table 5
Mole fraction (χ), particle size and dispersion of Co(fcc) and Co(hcp) for Stage 3 (Post-FTS).

Catalyst	Mole ratio (χ)			Particle size (nm)				Dispersion (%)		
	FCC Co^0	HCP Co^0	CoO	FCC Co^0	HCP Co^0		CoO	FCC Co^0	HCP Co^0	Weighted sum
					P_{II}	$P_{\perp}$				
Co/MCM-41	0.31	0.54	0.15	6.7	3.4	5.4	8.4	14.4	21.5	18.9
Co/MCM-48	0.23	0.14	0.63	5.1	1.2	3.3	4.8	18.9	46.0	29.0
Co/Co-MCM-48	0.22	0.62	0.16	46.7	1.5	4.6	6.0	2.1	35.8	27.1
Co/HMS	0.41	0.14	0.45	6.7	3.0	6.3	5.5	14.4	21.0	16.1
Co/Co-HMS	0.20	0.77	0.03	2.8	1.9	10.5	7.2	3.4	23.5	19.3
Co/SBA-15	0.21	0.53	0.26	7.8	2.8	8.5	5.7	12.4	18.9	17.0
Co/Co-SBA-15	0.18	0.72	0.09	7.8	1.6	4.9	6.2	12.4	32.6	28.5
Co/silica gel no. 775	0.42	0.44	0.14	17.2	3.1	6.2	6.4	5.6	20.7	12.7
Co/silica gel no. 646	0.35	0.64	0.01	18.5	3.1	5.8	4.2	5.2	21.5	15.8

ence of any additional amorphous cobalt species. Fig. 7A displays Co $L_{3,2}$-edge XANES spectra for a selection of catalysts at Stage 1. Irrespective of the support used, the data suggests that the cobalt species observed via XANES is Co_3O_4, with little to no contribution from other cobalt species. In particular, there is no significant difference between the impregnated catalysts with and without cobalt in the framework. Selected area diffraction patterns in TEM also confirmed the Co_3O_4 phase.

Fig. 7B compares L_3-edge XANES spectra for selected catalysts at Stages 2 and 3 with reference spectra and theoretical spectra. We expect the XANES data to be a linear combination of both metallic Co and CoO. The L_3-edge for the metal appears at 777.5 eV, while that for CoO is shifted to 779 eV with a pre-edge shoulder at 776 eV. The XANES spectra are qualitatively consistent with the XRD data analysis. For example, in the cobalt-HMS catalyst tested after reduction (Stage 2), a large peak appears at 779 eV which, when compared to the CoO standard, is in the energy range for CoO. The strength of this peak suggests a nearly equal amount of both metallic Co and CoO are present in our samples, similar to what was observed via XRD (Table 4). XANES simulations for CoO in both octahedral and tetrahedral coordination environments [53–55] were undertaken to see if there was any evidence for tetrahedrally-coordinated cobalt as might occur on surfaces. We observed fairly broad absorption edges in our samples, which might reflect some cobalt oxide in a non-octahedral coordination environment.

Table 6 shows the cobalt loading measured by inductively coupled plasma-mass spectrometry (ICP-MS), measured reaction rates, cobalt specific surface areas (assuming 14.6 Co atoms/nm^2), and calculated turnover frequencies for each supported catalyst. The reaction rates decrease with decreasing support pore diameter as shown in Fig. 8.

4. Discussion

The relationships between reactivity and catalyst support pore structure [9,15–17], cobalt particle size [8,10,11,25], cobalt particle reducibility [3,9,15] and transport properties [9,57–59] have been discussed extensively in the literature. In this work, we note a correlation between the specific activity of the catalysts examined and their pore diameter. We also observe a significant amount of a Co_{hcp} phase, consisting entirely of small cylindrical particles. Others have noted a relationship between pore diameter and CO conversion, frequently attributing it to the formation of larger, more easily reduced Co particles in larger pore materials [6,12,13,18,60,61], but also invoking mass transport limitations [9,62] or CO adsorption properties [60]. To try to better understand the relationship

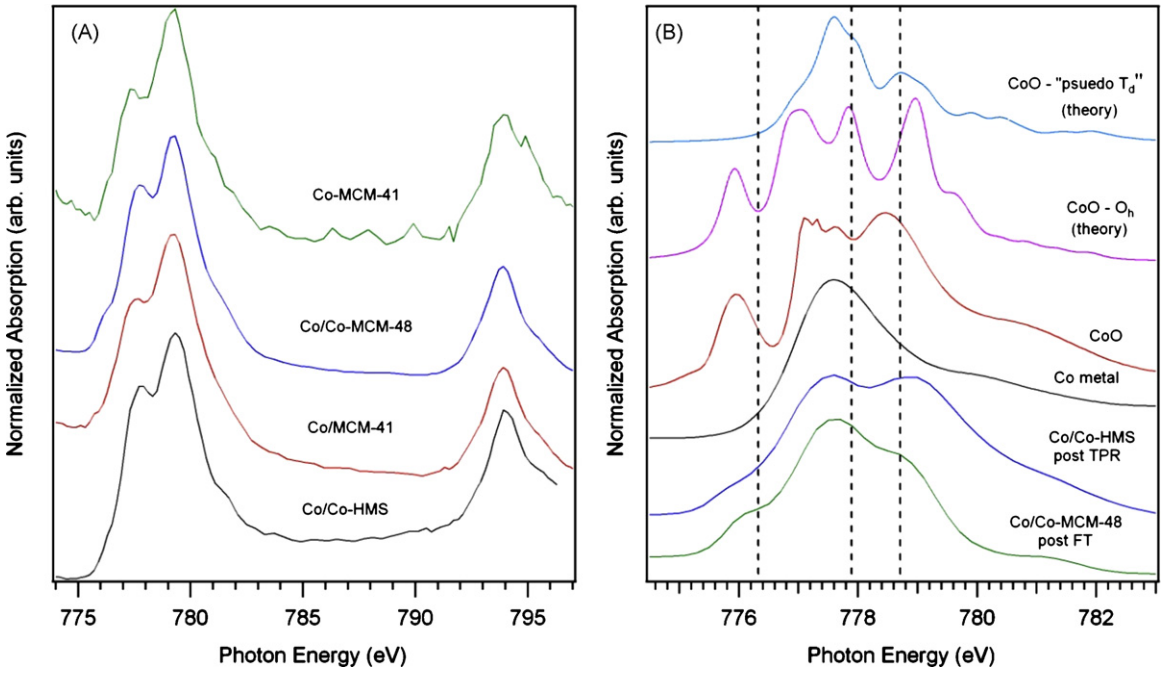

Fig. 7. Cobalt (A) $L_{3,2}$- and (B) L_3-edge XANES spectra for a selection of catalysts (A) after calcination to Co_3O_4 and (B) after reduction and FT reaction compared to reference and theory. All the spectra are normalized to unity at 777.6 eV (L3 peak maximum for metallic cobalt). The spectra for metallic cobalt and CoO were taken from Ref. [56].

Table 6
Catalysts, metal loading, reaction rate, specific surface areas (SSA) at each stage, and TOF.

Catalyst	Metal loading (%)	Reaction rate (10^{-6} mol/g Co s)	Co SSA (m^2/g) Stage 1	Co_{fcc} SSA (m^2/g Co) Stage 2	Co_{hcp} SSA (m^2/g Co) Stage 2	Co_{fcc} SSA (m^2/g Co) Stage 3	Co_{hcp} SSA (m^2/g Co) Stage 3	TOF (10^{-4} s^{-1})
Co/MCM-41	8.90	7.5	80	72	16	31	81	27.6
Co/MCM-48	7.50	5.04	52	29	23	30	45	27.7
Co/Co-MCM-48	8.25	9.95	15	5	89	3	155	25.9
Co/HMS	7.79	5.95	22	29	17	41	21	39.9
Co/Co-HMS	10.20	11.35	17	5	76	5	127	35.7
Co/SBA-15	9.38	20.7	76	17	70	18	70	99.1
Co/Co-SBA-15	10.10	5.97	48	5	199	16	164	13.7
Co/silica gel no. 775	9.11	23.8	70	48	35	16	64	139.7
Co/silica gel no. 646	9.06	25.2	47	14	67	13	96	95.2

between pore diameter and activity, we converted the specific activity data to turnover frequencies (TOF) by dividing the number of moles of carbon monoxide consumed by the number of sufficial Co atoms and then examined the relationships between TOF and pore diameter, Co phase composition, and Co_{hcp} and Co_{fcc} particle size.

We utilized a three-phase system to determine the specific surface area of metallic cobalt in each catalyst, which was then used to calculate TOFs. After activation and reduction (Stage 2) and after FTS (Stage 3), the catalyst properties (particle size and extent of reduction) were determined by XRD. In both Stages 2 and 3 all three cobalt phases were identified: Co_{fcc}, Co_{hcp} and CoO. We rely, in our analysis, primarily on data from XRD, with complementary information from nitrogen porosimetry, TEM/SAD, and XANES. XRD provides clear information on crystallites and their sizes but does not provide information on non-crystalline particles. XANES, on the other hand, is a local probe of electronic structure and does not require crystalline order for a signal. Therefore, cobalt $L_{3,2}$-edge XANES is a sensitive probe for analyzing non-crystalline cobalt species that may be present in our samples. XANES can also be used to qualitatively probe the level of reduction from Co_3O_4 to CoO and Co metal upon both TPR and FTS. Taken as a whole, the similarity in interpretations derived from our XRD and XANES measurements gives us confidence that relying on data from diffracting particles captures most of the cobalt chemistry occurring in these materials.

These results raise three key questions. First – how does the support pore size control the amount of CoO and the ease of reducibility of the Co_3O_4 catalyst precursor particles? Second – why are small hcp particles present and what impact do they have on the reactivity? Third – why are the turnover frequencies smaller in materials with small pore diameters? In addressing these questions, we review published information on pore diameters, particle size, reducibility and reactivity as well as on particle size and hcp/fcp formation and reactivity and then offer additional comments based on the novel observations reported here.

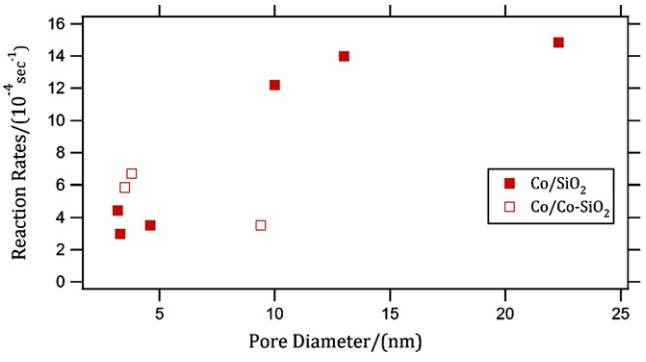

Fig. 8. Measured activity (reaction rates in (moles CO)/[(g Co-cat) s]) for catalysts as a function of pore diameter.

4.1. Dependence of the reducibility of CoO to Co on particle size

Smaller pore diameter supports show more CoO in both Stages 2 and 3, with the striking exception of Co/MCM-41. While oxidation has been postulated as a possible deactivation mechanism for FTS [9,17,45,63,64], in our materials we believe the presence of high mole fractions of CoO reflects the materials' intransigence to reduction. In fact, from Stages 2 to 3, the materials that had the highest mole fractions of CoO show reduction of CoO during FTS while materials that initially had less CoO show some oxidation. Formation of CoO between Stages 2 and 3 also correlates with the Co_{fcc} surface area: materials with more Co_{fcc} surface area in Stage 2 show an increase in mole fraction of CoO during FTS.

For small catalyst crystallites, particle size is known to alter the chemical equilibrium. As Co crystallites become smaller (i.e. ~10 nm), the contribution of surface energy to the chemical potential of the bulk material becomes significant, making reduction more difficult [65]. Additionally, for smaller pore diameter supports, diffusive effects may be important. Even at pressures of 7500 Torr, as in our experiments, the Knudsen number (defined as $K_n = \lambda/d$ where λ is the mean free path of the gas molecule and d is the pore diameter) is approximately 6, indicating a Knudsen diffusion regime. For Knudsen diffusion the diffusivity of a gas molecule scales with the root of molecular weight, thus pH_2O/pH_2 could increase by a factor of three. Given these facts, it is plausible that nanosized Co_3O_4 particles in mesopores could be more difficult to reduce beyond CoO [3,5]. Thus, the main trend in the mole fraction of CoO with pore diameter appears to be well explained by the size of clusters and the constraint of the pores. We see no evidence in the XANES data for non-crystallized cobalt silicate, whose presence has been postulated to decrease the reducibility of cobalt ions [66].

4.2. Relationships between Co(fcc) and Co(hcp) phases

At room temperature, the hcp phase should be the preferred phase, but under our treatment and reaction conditions, metastable fcc particles commonly occur [67,68]. Bulk cobalt metal undergoes a martensitic transformation, changing from hcp to fcc when heated above 693 K [67,69]. For smaller particles, phase transformation becomes more difficult because the increased surface energy of hcp particles favors the fcc structure [29,67]. Experimental results indicated that Co_{fcc} particles as large as 200 nm remained stable upon cooling to room temperature [69]. In our catalysts we see Co_{fcc} particles with diameters less than 20 nm, consistent with calculations of Kitakami et al. [67]. However, we also find small Co_{hcp} particles after the 773 K reduction step, which is not predicted. These Co_{hcp} particles remain stable through both Stages 2 and 3. The Co_{hcp} particles could form upon heating up to the transition temperature in hydrogen (cobalt oxide reduction) and remain in the Co_{hcp} phase at elevated temperatures, stabilized by their environment. An alternative could be that the particles form as Co_{fcc} then transition to Co_{hcp} upon cooling and during FT reaction.

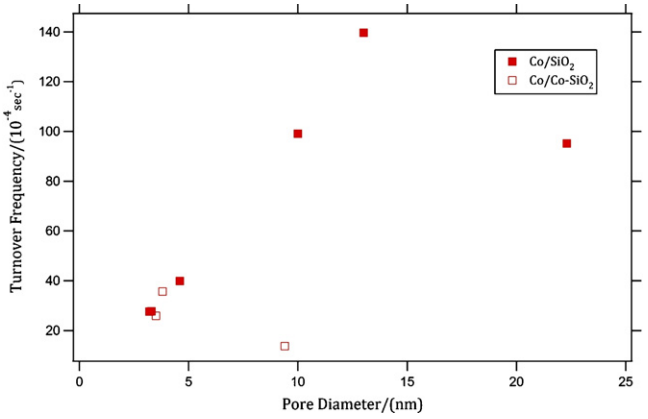

Fig. 9. Plot of turnover frequency vs. pore diameter.

In either case, we postulate that the environment surrounding the Co_{hcp} particles is energetically favorable for stabilization. The driving force for the bulk transformation is small, $-16\,J\,mol^{-1}$, therefore it is plausible that subtle changes in environment could provide the required energy to stabilize a particular phase [69]. We note that the mole fraction of Co_{hcp} is particularly high in the MCM-41, suggesting that the environment stablizes the hcp phase so strongly that it is even favored over the CoO phase, perhaps accounting for the low amount of CoO.

The highly reproducible particle shape anisotropy and preferential orientation is another indication that abnormally small Co_{hcp} particles are stabilized in the silica pores. The XRD analysis is consistent with disc-shaped particles (i.e. cylinders whose diameter is twice its height) which, in comparison to spherical particles, have a 21% increase in surface area to volume ratio. Observation of preferential orientation suggests that the high index facets are in contact with pore walls in order to lower surface energies. The connection between Co_{hcp} stabilization and secondary meso/micropores in silica supports requires further investigation.

Prior work has suggested Co nanocrystals can contain hcp domains within a larger particle [20,21,70–72]. Our TEM data is inconsistent with that interpretation for the catalysts described in this paper. We observe that the hcp particle size is relatively indifferent to the size of the fcc particles in the various materials synthesized, which also seems unlikely to be consistent with the interpretation that the hcp particles are embedded in larger fcc particles.

4.3. Relationship between TOF and pore diameter

The turnover frequencies were calculated using the cobalt loading, measured reaction rate at the end of the FT reaction, and a mole fraction weighted sum of the dispersions of each Co metal phase (Stage 3). There is a linear relationship between TOF and pore diameter up to a pore diameter of 13 nm, as shown in Fig. 9. At pore diameters larger than 13 nm, it appears that TOF is insensitive to pore diameter (see Fig. 9), or perhaps that it even decreases. This analysis suggests three possibilities: (1) the Co phase is intrinsically more active in the larger pore materials to the extent that larger pores contain larger metal particles, which have higher activity; (2) wide pore catalysts have more CO adsorption sites [60] or (3) the diffusion of reactants and products is faster with larger pore materials [57]. We favor the latter interpretation because the majority of the surface area comes from hcp particles, whose size does not vary much (Fig. 6), and the amount of it shows no correlation with pore size (see Fig. 5). The size of Co_{fcc} particles does generally increase with pore diameter, but the mole fraction of fcc is similar in magnitude to that of the hcp. This data argues against a particle size

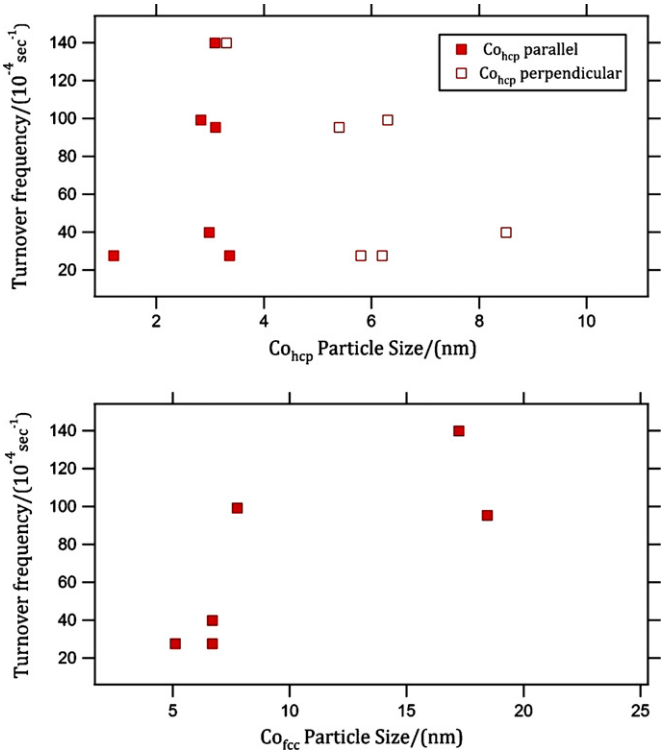

Fig. 10. (A) TOF vs. Co_{hcp} particle size and (B) TOF vs. Co_{fcc} particle size.

effect. Iglesia et al. point out that CO diffusion can limit reaction rates for 1–3 mm catalyst particles [58] and that particles smaller than 200 μm are necessary to avoid diffusional limitations. Our particles range in size from 180 to 400 μm. However it is possible that a combination of factors contribute to the reactivity reported here. We note also that there is an inverse relationship between TOFs and surface area.

A decrease in TOF below a critical particle size has been interpreted to mean that the reaction is sensitive to the structure of the cobalt metal, whereas if the TOF is independent of particle size then neither electronic effects nor defect sites affect the intrinsic reaction rate of the catalyst particle. In a number of FT studies, the TOF decreases below a particle size of about 8 nm [9–11]. Because our catalysts are comprised of two phases – a Co_{fcc} phase in which particle size does scale with pore diameter and a Co_{hcp} phase that is uniformly made up of small particles whose size does not vary with pore diameter – it is not surprising that there is no clear correlation between particle diameter and TOF. We plot TOF vs. particle size for both the Co_{fcc} and Co_{hcp} particles (Fig. 10) and see no trend between TOF and the size of the Co_{hcp} particles. We do, however, see a correlation between Co_{fcc} particle size and TOF, but the Co_{fcc} particles make a small contribution to the overall surface area of metallic cobalt so it is unlikely that Co_{fcc} particles are determining reactivity. Rather the relationship between Co_{fcc} particle size and TOF is likely to be simply a function of the fact that the Co_{fcc} particle size scales with pore diameter and pore diameters and TOFs are correlated.

A number of groups have determined dispersion from either the Co_3O_4 particle size after calcination [9,73] or the Co_{fcc} particle size after reduction or post-reaction [20]. In Fig. 11, we plot the Co_{fcc} and Co_{hcp} particle sizes determined at Stages 2 and 3, respectively from XRD against the particle size estimated from Co_3O_4 particles at Stage 1. Co_{fcc} and Co_3O_4 particle sizes are correlated but there is essentially no correlation between Co_{hcp} particle sizes and Co_3O_4 particles size estimates. The large mole fraction and high dispersion of the Co_{hcp} phase (dispersions of 20–50% in our catalysts) produces

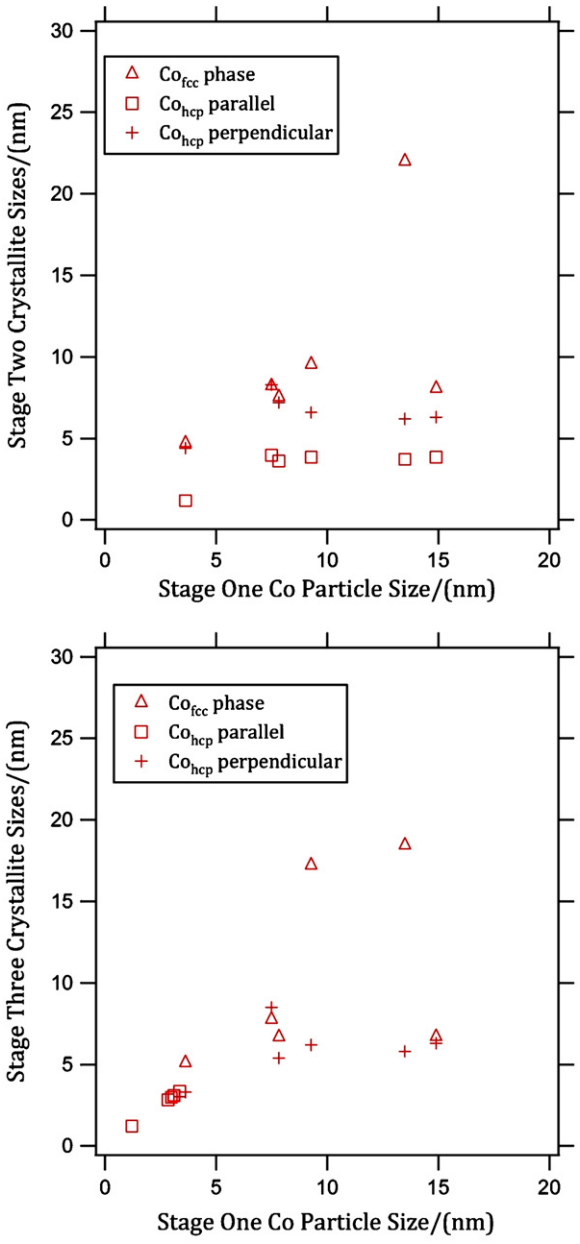

Fig. 11. Relationship between Co metal particle size estimated from Co_3O_4 and particle sizes of fcc and hcp particles determined (A) after reduction (Stage 2) or (B) after FT synthesis (Stage 3), showing that there is a strong correlation between Co_3O_4 particle size and Co_{fcc} particle size, but no correlation with Co_{hcp} size.

large hcp specific surface areas. If the hcp phase is as active as the fcc phase, then our specific surface areas would suggest that as much as 95% of the reaction could take place on the hcp phase. Thus, calculations of TOF that neglect the Co_{hcp} content and base dispersion on total (reduced) metal content and the Co_{fcc} dispersion (from XRD), could generate overly optimistic estimates of intrinsic reaction rates.

Annealing Co-containing materials at high temperature under a hydrogen atmosphere has been shown to change the cobalt dispersion [24]. Whether the particles become larger or smaller (as well as the extent of any phase changes) is likely to depend on the precise conditions of FTS. We provide evidence that both particle size and Co phases depend on treatment conditions [20]. Our data are consistent with a model in which small hcp particles can be stabilized in mesoporous materials, despite high thermal treatment and these small particles can, when present, contribute significantly to the total fraction of Co in a catalyst. Our data is also consistent with a model in which the Co_{fcc} particles contribute to the catalytic activity. In some materials, a fraction of these particles may be on the exterior surfaces of the silicas and not inside the pores, although our data shows no clear consequence of the presence of a small fraction of surface particles.

The post-reaction characterization of the materials shows a strong correlation between TOF and pore diameter (see Fig. 9). It seems likely that larger pores (up to approximately 13 nm) facilitate diffusion of reactants and products, thereby speeding up reaction rates. Larger pores are also less prone to occlusion and oxidative inactivation.

5. Conclusion

We have synthesized and characterized silica supported cobalt catalysts with different pore diameters for evaluation in the Fischer–Tropsch reaction. Our characterization included determining detailed catalyst properties at three stages of catalyst history: (1) after the initial oxidation step to thermally decompose the catalyst precursor, (2) after the hydrogen reduction step to activate the catalyst and (3) after FT reaction. The careful use of XRD analysis allowed the particle size of each Co phase, fcc and hcp, to be determined as well as the quantification of the amounts of each phase. The particle sizes of the Co_{fcc} decreased with decreasing support pore size whereas the particle size of Co_{hcp} remained constant and anisotropic in shape for Stages 2 and 3. The Co_{hcp} particle size was consistently smaller than the Co_{fcc} particle size. The CoO mole fraction is larger with smaller pore materials, indicating that those materials are more difficult to fully reduce. We find a very good correlation between pore diameter and TOF with a maximum TOF occurring at materials with a pore diameter around 13 nm.

Acknowledgements

The authors acknowledge the financial support of DOE Epscor Grant #DE-FG02-07ER46373. This grant has enabled the development of the infrastructure necessary for the initiation of a new research effort in the thermal conversion of woody biomass to fuels and chemicals. The authors also acknowledge contributions from Nick Hill, Kelly Edwards, Tessa Pals and David Frankel.

References

[1] A.Y. Khodakov, W. Chu, P. Fongarland, Chemical Reviews 107 (2007) 1692–1744.
[2] E. van Steen, M. Claeys, Chemical Engineering & Technology 31 (2008) 655–666.
[3] H. Li, S. Wang, F. Ling, J. Li, Journal of Molecular Catalysis A: Chemical 244 (2006) 34–40.
[4] R. Ravishankar, M.M. Li, A. Borgna, Catalysis Today 106 (2005) 149–153.
[5] E. Lira, C.M. Lopez, F. Oropeza, M. Bartolini, J. Alvarez, M. Goldwaser, F.L. Linares, J.-F. Lamonier, M.J.P. Zurita, Journal of Molecular Catalysis A: Chemical 281 (2008) 146–153.
[6] Y. Ohtsuka, Y. Takahashi, M. Noguchi, T. Arai, S. Takasaki, N. Tsubouchi, Y. Wang, Catalysis Today 89 (2004) 419–429.
[7] A. Khodakov, Catalysis Today 144 (2009) 251–257.
[8] O. Borg, P.D.C. Dietzel, A.I. Spjelkavik, E.Z. Tveten, J.C. Walmsley, S. Diplas, S. Eri, A. Holmen, E. Ryttera, Journal of Catalysis 259 (2008) 161–164.
[9] A. Khodakov, A. Griboval-Constant, R. Bechara, V. Zholobenko, Journal of Catalysis 206 (2002) 230–241.
[10] G.L. Bezemer, J.H. Bitter, H. Kuipers, H. Oosterbeek, J.E. Holewijn, X.D. Xu, F. Kapteijn, A.J. van Dillen, K.P. de Jong, Journal of the American Chemical Society 128 (2006) 3956–3964.
[11] A. Martinez, G. Prieto, Journal of Catalysis 245 (2007) 470–476.
[12] J. Hong, P.A. Chernavskii, A. Khodakov, W. Chu, Catalysis Today 140 (2009) 135–141.
[13] A. Khodakov, R. Bechara, A. Griboval-Constant, Applied Catalysis A: General 254 (2003) 273–288.
[14] W. Chu, P.A. Chernavskii, L. Gengembre, G. Pankina, P. Fongarland, A. Khodakov, Journal of Catalysis 252 (2007) 215–230.
[15] H.L. Li, S.G. Wang, F.X. Ling, J.L. Li, Journal of Molecular Catalysis A: Chemical 244 (2006) 33–40.

[16] A.M. Saib, M. Claeys, E. van Steen, Catalysis Today 71 (2002) 395–402.
[17] H.L. Li, J.L. Li, H.K. Ni, D.C. Song, Catalysis Letters 110 (2006) 71–76.
[18] O. Gonzalez, H. Perez, P. Navarro, L.C. Almeida, J.G. Pacheco, M. Montes, Catalysis Today 148 (2009) 140–147.
[19] D. Song, J. Li, Journal of Molecular Catalysis A: Chemical 247 (2006) 206–212.
[20] O. Ducreux, B. Rebours, J. Lynch, M. Ray-Auberger, D. Bazin, Oil and Gas Science and Technology – Revue de l'IFP 64 (2009) 49–62.
[21] D.I. Enache, B. Rebours, M. Roy-Auberger, R. Revel, Journal of Catalysis 205 (2002) 346–353.
[22] R. Srinivasan, R.J. De Angelis, P.J. Reucroft, A.G. Dhere, J. Bentley, Journal of Catalysis 116 (1989) 144–163.
[23] J. Panpranot, J.G.J. Goodwin, A. Sayari, Catalysis Today 77 (2002) 269–284.
[24] G. Prieto, A. Martinez, R. Murciano, M. Arribas, Applied Catalysis A: General 367 (2009) 146–156.
[25] J.P. den Breejen, P.B. Radstake, G.L. Bezemer, J.H. Bitter, V. Froseth, A. Holmen, K.P. de Jong, Journal of the American Chemical Society 131 (2009) 7197–7203.
[26] C.Y. Chen, H.X. Li, M.E. Davis, Microporous Materials 2 (1993) 17–26.
[27] K. Schumacher, M. Grun, K.K. Unger, Microporous and Mesoporous Materials 27 (1999) 201–206.
[28] A. Tuel, Microporous and Mesoporous Materials 27 (1999) 151–169.
[29] Z.H. Luan, M. Hartmann, D.Y. Zhao, W.Z. Zhou, L. Kevan, Chemistry of Materials 11 (1999) 1621–1627.
[30] D.Y. Zhao, J.Y. Sun, Q.Z. Li, G.D. Stucky, Chemistry of Materials 12 (2000) 275–279.
[31] J.B. Rosenholm, H. Rahiala, J. Puputti, V. Stathopoulos, P. Pomonis, I. Beurroies, K. Backfolk, Colloids and Surface A: Physicochemical and Engineering Aspect 250 (2004) 289–306.
[32] H. Golinska, P. Decyk, M. Ziolek, J. Kujawa, E. Filipek, Catalysis Today 142 (2009) 175–180.
[33] D.S.-G. Fuentes-Perujo, J. Mérida-Robles, E. Rodríguez-Castellón, A. Jiménez-López, P. Maireles-Torres, R. Moreno-Tost, R.J. Mariscal, Journal of Solid State Chemistry 179 (2006) 2182–2189.
[34] Y. Xia, R Mokaya, Journal of Materials Chemistry 14 (2004) 3427–3435.
[35] B. Dragoi, E. Dumitriu, C. Guimon, A. Auroux, Microporous Mesoporous Mater 121 (2009) 7–17.
[36] T. Chiranjeevi, G. Muthu Kumaran, J.K. Gupta, G. Murali Dhar, Thermochimica Acta 443 (2006) 87–92.
[37] N. Kob, R.S. Drago, V. Young, Inorganic Chemistry 36 (1997) 5127–5131.
[38] M.T. Bore, M.P. Mokhonoana, T.L. Ward, N.J. Coville, A.K. Datye, Microporous and Mesoporous Materials 95 (2006) 118–125.
[39] M.T. Bore, T.L. Ward, R.F. Marzke, A.K. Datye, Journal of Materials Chemistry 15 (2005) 5022–5028.
[40] G. Xomeritakis, C.Y. Tsai, J.B. Jiang, C.J. Brinker, Journal of Membrane Science 341 (2009) 30–36.
[41] S. Battersby, S. Smart, B. Ladewig, S. Liu, M.C. Duke, V. Diniz da Costa, Separation and Purification Technology 66 (2009) 299–305.
[42] S. Brunauer, P.H. Emmett, E. Teller, Journal of the American Chemical Society 60 (1938) 309–319.
[43] E.P. Barrett, L.G. Joyner, P.P. Halenda, Journal of the American Chemical Society 73 (1951) 373–380.
[44] M. Kruk, M. Jaroniec, A. Sayari, Langmuir 13 (1997) 6267–6273.
[45] J. van de Loosdrecht, B. Balzhinimaev, J.A. Dalmon, J.W. Niemantsverdriet, S.V. Tsybulya, A.M. Saib, P.J. van Berge, J.L. Visagie, Catalysis Today 123 (2007) 293–302.
[46] A.M. Saib, D.J. Moodley, I.M. Ciobica, M.M. Hauman, B.H. Sigwebela, C.J. Weststrate, J.W. Niemantsverdriet, J.V.D. Loodscrecht, Catalysis Today 154 (2010) 271–282.
[47] A.M. Saib, A. Borgna, J. van de Loosdrecht, P.J. van Berge, J.W. Geus, J.W. Niemantsverdriet, Journal of Catalysis 239 (2006) 326–339.
[48] B.H. Toby, Journal of Applied Crystallography 34 (2001) 210–213.
[49] A.C. Larson, R.B. Von Dreele, General Structure Analysis System (GSAS) Manual, LANSCE, MS-H805, Los Alamos National Laboratory, Los Alamos, NM, 1994.
[50] R. Speight, A. Wong, P. Ellis, T. Hyde, P.T. Bishop, M.E. Smith, Solid State Nuclear Magnetic Resonance 35 (2009) 67–73.
[51] A. Martinez, C. Lopez, F. Marquez, I. Diaz, Journal of Catalysis 220 (2003) 486–499.
[52] A. Khodakov, V. Zholobenko, R. Bechara, D. Durand, Microporous and Mesoporous Materials 79 (2005) 29–39.
[53] F.M.F. de Groot, J.C. Fuggle, B.T. Thole, G.A. Sawatzky, Physical Review A 42 (1990) 5459–5468.
[54] F.M.F. de Groot, Coordination Chemistry Reviews 249 (2005) 31.
[55] F.M.F. de Groot, M. Abbate, J. van Elp, G.A. Sawatzky, Y.J. Ma, C.T. Chen, F. Sette, Journal of Physics Condensed Matter 5 (1993) 2277–2288.
[56] T.J. Regan, H. Ohldag, C. Stamm, F. Nolting, J. Lüning, J. Stöhr, R.L. White, Physical Review B 64 (2001) 214422–214433.
[57] A. Martinez, G. Prieto, J. Rollan, Journal of Catalysis 263 (2009) 292–305.
[58] E. Iglesia, S. Soled, J.E. Baumgartner, S.C. Reyes, Journal of Catalysis 153 (1995) 108–122.
[59] E. Iglesia, Applied Catalysis A: General 161 (1997) 59–78.
[60] H. Xiong, Y. Zhang, K. Liew, J. Li, Journal of Molecular Catalysis A: Chemical 295 (2008) 68–76.
[61] A.Y. Khodakov, A. Griboval-Constant, R. Bechara, V.L. Zholobenko, Journal of Catalysis 206 (2002) 230–241.
[62] R.B. Anderson, W.K. Hall, A. Krieg, B. Seligman, Journal of the American Chemical Society 71 (1949) 183–188.
[63] A.M. Saib, A. Borgna, J.V. De Loosdrecht, P.J. Van Berge, J.W. Niemantsverdriet, Journal of Physical Chemistry B 110 (2006) 8657–8664.
[64] D. Schanke, A.M. Hilman, E. Bergene, K. Kinnari, E. Rytter, E. Adnanes, A. Holmen, Energy and Fuels 10 (1996) 867–872.
[65] E. van Steen, M. Claeys, M.E. Dry, J. van de Loosdrecht, E.L. Viljoen, J.L. Visagie, Journal of Physical Chemistry B 109 (2005) 3575–3577.
[66] B. Ernst, S. Libs, P. Chaumette, A. Kiennemann, Applied Catalysis A: General 186 (1999) 145–168.
[67] O. Kitakami, H. Sato, Y. Shimada, F. Sato, M. Tanaka, Physical Review B 56 (1997) 13849.
[68] X.J. Yin, K. Peng, A.P. Hu, L.P. Zhou, J.H. Chen, Y.W. Du, Journal of Alloys and Compounds 479 (2009) 372–375.
[69] X.Q. Zhao, S. Veintemillas-Verdaguer, O. Bomati-Miguel, M.P. Morales, H.B. Xu, Physical Review B 69 (2005) 24106–24113.
[70] C. Desgrange, J. Delhommelle, Journal of Physical Chemistry B 111 (2007) 1465–1469.
[71] V. Dureil, C. Ricolleau, M. Gandais, C. Grigis, European Physical Journal D: Atomic, Molecular, and Optical Physics 14 (2001) 83–88.
[72] V.F. Puntes, K.M. Krishnan, A.P. Alivisatos, Science 291 (2001) 2115–2117.
[73] D. Schanke, W. Vada, E.A. Blekkan, A.M. Hilmen, A. Hoff, A. Holmen, Journal of Catalysis 156 (1995) 85–95.